Journal of Catalysis 429 (2024) 115209

Contents lists available at ScienceDirect

Journal of Catalysis

journal homepage: www.elsevier.com/locate/jcat

Optimizing the use of a gas diffusion electrode setup for CO_2 electrolysis imitating a zero-gap MEA design

Shima Alinejad [a], Jonathan Quinson [b,c], Yao Li [d], Ying Kong [a], Sven Reichenberger [d], Stephan Barcikowski [d], Peter Broekmann [a], Matthias Arenz [a,*]

[a] University of Bern, Department of Chemistry, Biochemistry and Pharmaceutical Sciences, Freiestrasse 3, 3012 Bern, Switzerland
[b] University of Copenhagen, Department of Chemistry, Universitetsparken 5, 2100 Copenhagen Ø, Denmark
[c] Biochemical and Chemical Engineering Department, Åbogade 40, 8200 Aarhus, Denmark
[d] University of Duisburg-Essen, Technical Chemistry I and Center of Nanointegration Duisburg-Essen (CENIDE), Universitätsstraße 7, Essen, North Rhine-Westphalia 45141, Germany

ARTICLE INFO

Keywords:
Gas diffusion electrode
CO_2 reduction
Electrolysis

ABSTRACT

The lack of a robust and standardized experimental test bed to investigate the performance of catalyst materials for the electrochemical CO_2 reduction reaction (ECO_2RR) is one of the major challenges in this field of research. To best reproduce and mimic commercially relevant conditions for catalyst screening and testing, gas diffusion electrode (GDE) setups attract rising attention as an alternative to conventional aqueous-based setups such as the H-cell configuration. Zero-gap electrolyzer designs show promising features for upscaling to the commercial scale. In this study, we scrutinize further our recently introduced "zero-gap GDE" setup or more correct half-cell MEA design for the CO_2RR. Using an Au electrocatalyst as a model system we simulate the anode conditions in a zero-gap electrolyzer and identify/report the key experimental parameters to control the catalyst layer preparation to optimize the activity and selectivity of the catalyst. Among others, it is demonstrated that supported Au nanoparticles (NPs) result in significantly higher current densities when compared to unsupported counterparts, however, the supporting also renders the NPs prone to agglomeration during electrolysis.

1. Introduction

Climate change and the associated global rise in Earth's average temperature have emerged as paramount concerns in recent decades [1]. Among the leading contributors to this climate change is the steep rise in atmospheric carbon dioxide (CO_2) levels [2]. In response, society is actively pursuing strategies aimed at mitigating and significantly reducing CO_2 emissions. These strategies include transitioning to renewable energy sources and embracing electric and fuel-cell vehicles. Beyond conventional mitigation approaches, a notable area of research centers on harnessing CO_2 as a feedstock for the CO_2 reduction reaction (CO_2RR) to produce fuels and value-added chemicals such as carbon monoxide (CO), formic acid, ethylene, ethanol, methane, and methanol [3]. One of the key challenges in the field of CO_2RR research is the lack of a standard experimental setup and methodology to rapidly screen the performances of various catalytic materials that hold promise as catalysts in CO_2RR technology development [2]. Commonly used screening methods for CO_2RR can be broadly categorized into two main groups: aqueous-fed systems and gas-diffusion electrode (GDE) setups [4]. Aqueous-fed systems such as the H-cell configuration, Fig. 1-a, have the disadvantage of low solubility of CO_2 which limits the CO_2 conversion [5,6]. In contrast, GDE setups circumvent this limitation by continuously supplying CO_2 gas to the catalyst layer enabling high current densities. Transitioning from an H-cell to a GDE setup, the CO_2 diffusion pathway to the surface of the catalyst is reduced by roughly three orders of magnitude, from ≈ 50 μm in an H-cell to ≈ 50 nm in a GDE setup. This leads to a substantial increase in maximum achieved current densities in GDE setups [4].

Despite these advantages of GDE setups, classical H-cell configurations are employed in the majority (>95 %) [7,8] of fundamental studies for CO_2RR catalytic materials development and characterization [4]. Emerging screening methods for CO_2RR based on GDE setups can be sub-divided into microfluidic designs [9–11] and "zero-gap half-cell" designs [5,8,12–15]. Fig. 1-b, shows a design sometimes referred to "Kenis-type" [4] with a flowing catholyte, Fig. 1-c, a "zero-gap half-cell" design where a gas diffusion layer (GDL), catalyst and polymer exchange

* Corresponding author.
E-mail address: matthias.arenz@unibe.ch (M. Arenz).

https://doi.org/10.1016/j.jcat.2023.115209
Received 29 June 2023; Received in revised form 5 November 2023; Accepted 14 November 2023
Available online 19 November 2023

membrane are combined as one unit without presence of a liquid electrolyte separating the cathode layer from the polymer exchange membrane. The aim is to simulate the conditions at the cathode of a zero-gap electrolyzers without significant interference of the anode. It should be noted that several different microfluidic designs can be found, and often both catholyte and anolytes are circulated in and out the cell. Their absolute and relative flow is indeed a very important parameter to regulate local built-in pressure and operation. Further literature on GDE designs and comparisons of the performance in respective cells can be found in refs. [16–21].

Zero-gap electrolyzers are also known as polymer electrolyte membrane (PEM) electrolyzers, catholyte-free, or gas-phase electrolyzers. Using gas diffusion layers on both electrodes of the reactor, Fig. 1-d, in the same way as in membrane electrode assemblies (MEAs) for fuel cells, the CO_2RR can be enhanced since a better distribution and higher pressure of CO_2 can be reached due to the porous electrodes. Hence the performance is improved [22,23]. The advantages of zero-gap electrolyzers over the designs containing liquid electrolyte are multiple: it is relatively easy to pressurize the reactant and product flows, no product separation from the catholyte is required. In addition, the similarity of these devices to PEM water electrolyzers makes it easier to scale up to the commercial scale and construct the large sized stacks then required [7]. However, due to the lack of an electrolyte between the catalyst layer and polymer exchange membrane in zero-gap electrolyzers, this design may suffer from CO_2 reduction selectivity [5,24]. It has been reported that the selectivity problem in zero-gap CO_2 electrolyzers can be promisingly mitigated in the presence of liquid electrolyte or water in the porous catalyst layer [6]. Recently, an optimization of several operational parameters related to cathode water management showed that water management is indeed key in the operation of zero-gap electrolyzers. High water input was reported to lead to flooding of the electrodes, whereas lower values were reported to decrease the performance of the anion exchange membrane and reduce catalyst wetting [25].

In this study, we implemented our in-house developed GDE setup with a half-cell design simulating zero-gap electrolyzers to conduct CO_2 electrolysis using a standard gold (Au) electrocatalyst. The advantages of this "zero-gap" GDE setup have previously been demonstrated in a screening of Au nanoparticle (NP) catalysts to assess their selectivity and activity towards the CO_2RR under industrially relevant current densities [26]. Notably, prior research by Gálvez-Vázquez et al. [27], revealed that that prolonged use of a silver (Ag) based catalyst, can result in limitations due to bicarbonate precipitations affecting selectivity and causing performance decline. This phenomenon was corroborated in a recent study by Kong et al. [28], which examined the influence of various gas diffusion layers (GDLs) on the performance decay of an Ag-based catalyst layer in this setup. The research indicated that cracks in the setup play a significant role in electrolyte management and help mitigate performance degradation due to flooding.

Our current study aims to further explore the factors impacting CO_2RR performance. We employed an Au based catalyst as an alternative for Ag when targeting CO as reaction product. Using the same setup, we conducted a screening study to investigate several influences affecting the performance. To isolate influences specific to the GDE approach, we replicated the experiments in both the GDE and H-cell configurations, under conditions typical for each setup — alkaline conditions in the GDE setup and bicarbonate electrolyte in the H-cell setup. Through optimization of parameters such as membrane, humidification, and the application of supporting NPs onto carbon, we enhanced the activity and selectivity of the catalyst in the GDE cell. Additionally, we introduced a new technique to highlight the agglomeration of Au NPs as a potential degradation mechanism. Small-angle X-ray scattering (SAXS) enabled us to track particle size changes before and after CO_2 electrolysis. Our observations confirm that the utilization of the GDE setup presents several challenges unrelated to the active catalyst phase. Addressing these challenges is crucial when seeking to scale up the process.

2. Experimental

2.1. Preparation of 25 wt% Au supported on carbon (Au/C)

3 mg of carbon Vulcan (XC72R, Fuel cell store) was added to 6.65 mL of ethanol (Ethanol absolute, VWR chemicals). After stirring for 5 min in the ultrasonic bath, the mixture was further dispersed using a horn sonicator (Q500, QSonica, 500 W, 20 kHz) with a pulse of 1 s working and 1 s resting for 10 min to achieve a homogenous carbon dispersion. In this study, we used surfactant free colloidal Au NPs in water as a solvent, which were synthesized based on a laser ablation method [26]. The particle size of the colloidal Au NPs was ca. 8 nm After adding 13.3 mL of the Au NPs colloidal suspension (1 mg of Au) to the carbon suspension, the mixture was stirred for 10 min by means of the horn sonicator. Finally, the glass vial containing the mixture was placed openly under a hood for solvent evaporation for around 5 days. After the first 24 h, a black precipitation was observed on the bottom of the glass vial.

2.2. Preparation of the catalyst ink

2.2.1. Unsupported Au NPs

13.3 mL of the unsupported Au NPs colloidal (1 mg of Au), and 2.6 µL of the 10 wt% Nafion ionomer (D1021, 10 wt% in H_2O, EW 1100, Fuel Cell Store) were mixed with 13.2 mL of isopropanol (IPA, 99.7+%, Alfa

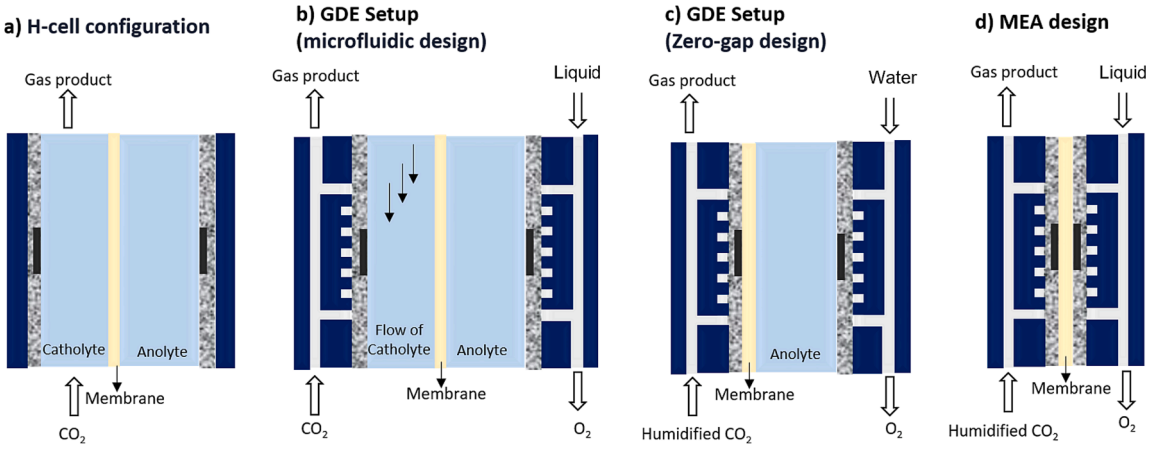

Fig. 1. Schematic of commonly used configurations for screening CO_2RR. (a) H-cell configuration, (b) microfluidic design of GDE setup with a flowing catholyte channel, (c) zero-gap GDE setup with a non-flowing catholyte, and (d) MEA design of a zero gap electrolyzer.

Aesar). The glass vial containing the mixture was sonicated in the ultrasonic bath for 15 min.

2.2.2. 25 wt% supported Au on carbon (Au/C)

For the preparation of the catalyst ink, ultrapure Milli-Q water (resistivity > 18.2 MΩ cm, total organic carbon (TOC) < 5 ppb) from a Milli-Q system (Millipore) was used. 13.3 mL of IPA: Milli-Q water (3:1, v:v) mixed solvent was added to a glass vial containing 4 mg of 25 wt% Au/C. The glass vial containing the mixture was sonicated in the ultrasonic bath for 15 min. For the preparation of the catalyst ink formulation of supported Au/C, different amounts of Nafion ionomer (D1021, 10 wt % in H_2O, EW 1100, Fuel Cell Store) and Anion ionomer (Sustainion XA-9 Alkaline Ionomer 5 % in ethanol, Dioxide Materials) were used, Table 1.

2.3. Preparation of the catalyst film

For the catalyst film preparation, the same vacuum filtration setup was used as reported in our previous work [26]. In this setup, a cylindrical reservoir with a cross-sectional area of 1.76 cm^2 was filled with 9.45 mL of the respective catalyst ink. Subsequently, a vacuum was applied by means of a Schlenk line pump thereby sucking the ink through a gas diffusion layer (GDL, H23C8 Freudenberg) which consisted of a macroporous (fibrous) layer and a microporous layer (MPL). Prior to filtration the GDL was positioned on a fritted glass filter. Thus, a homogenous catalyst layer was obtained, which was dried overnight in air. The nominal gold loading of the prepared Au films on the GDL, which we refer to as GDE, was 200 $\mu g_{Au}\ cm_{geo}^{-2}$. Prior to the catalyst film preparation the vacuum filtration setup was always soaked overnight in aqua regia solution followed by a gentle rinsing with water. In order to determine the real catalyst mass loading, the freshly prepared GDEs were subjected to an inductively coupled plasma-mass spectrometry (ICP-MS) analysis (Table 1). Technical details of this procedure are provided in in section 2.8. For the unsupported Au NPs, a particle loss during the vacuum filtration process was expected and confirmed by the ICP-MS analysis. It has also been observed that the presence of an ionomer in the catalyst ink leads to reduced particle losses during the catalyst film preparation. For all ionomer containing Au/C GDE samples the measured mass loadings, measured by ICP-MS, indeed matched with their nominal loadings. However, for those Au/C GDE samples which have been prepared without ionomers there was a substantial discrepancy observed between the measured mass loadings and the expected values. In addition, the high uncertainty values indicate a catalyst film preparation which is less reproducible compared to those cases where the ionomer was present.

2.4. Activation of membranes

For the activation of the anion exchange membrane, the membrane (Sustainion® X37-50 Grade RT Membrane, with a dry thickness of 50 μm thick, Dioxide Materials) was immersed in 1 M KOH for 24 h, and subsequently punched into circular pieces with a diameter of 2 cm by means of a sharp puncher. The punched and activated membranes were kept in a plastic bottle filled with 1 M KOH. For the activation of the Nafion membrane, after punching circles with a diameter of 2 cm from a sheet of Nafion membrane (Nafion 117, 183 μm thick, Fuel Cell Store), the punched membranes were treated for 30 min at 80 °C in 5 wt% H_2O_2, followed by 30 min at 80 °C in Milli-Q water and 30 min at 80 °C in 8 wt % H_2SO_4 solution. Between all treatments the membranes were rinsed thoroughly by Milli-Q water. The activated Nafion membranes were kept in a glass vial filled with Milli-Q water. For both anion exchange and Nafion membranes, the activated membrane was gently rinsed with ultrapure Milli-Q water before assembling it into the GDE setup, and thereafter dried with precision wipes (Kimtech science).

2.5. Preparation of GDE setup

The employed GDE setup has already been described elsewhere [27,29]. For the preparation of the working electrode (WE), a GDL without an MPL with diameter of 2 cm (H23, 170 μm thick @ 1 MPa, Freudenberg), a GDL with an MPL (H23C8, 200 μm thick @ 1 MPa, Freudenberg) with a diameter of 2 cm and a circle hole of 3 mm in the center that was filled with the punched Ø 3 mm GDE, and an activated membrane (Ø 2 cm), respectively, were placed on top of the flow field, between the lower cell body (stainless steel) and the upper cell body (polytetrafluoroethylene (PTFE)), Fig. 2-a. The active GDE with a diameter of 3 mm results in a geometric surface area of 0.07 cm^2. The activated membrane, which was placed on top of the GDE, separates the liquid electrolyte from the catalyst layer. Therefore, due to the lack of a flowing electrolyte between the catalyst layer and the ion- exchange membrane, this GDE setup configuration can be categorized as "zero-gap" or catholyte-free half-cell setup as the cathode (GDE) directly contacts the membrane. With the help of a stainless-steel clamp, the upper and lower cell body were pressed together as shown in Fig. 2-b. The PTFE upper cell body was filled with 15 mL of 2 M potassium hydroxide solution (KOH, Merck, pH≈14). A gold wire and a silver/silver chloride electrode (Ag/AgCl, 3 M KCl, VWR, double junction design) were used as the counter electrode (CE) and reference electrode (RE), respectively. To improve the reproducibility of the measurements, the CE was placed inside a separate compartment with a glass frit on the bottom, which is indicated as CE capillary. The cleaning of the cell was the same as described in our previous works [30,31]. For the humidification of the reactant gas, a glass bubbler filled with Milli-Q water was connected to the gas inlet of the lower cell body. During the electrolysis, a humidified CO_2 stream (16 mL min^{-1}) was continuously fed through the inlet of the GDE setup to transport the gaseous products from the outlet of GDE setup to the sample loop of the GC.

2.6. Assembly of the H-cell

A home-made gas-tight H-type glass cell was employed in this study, Fig. 3. The catholyte and the anolyte compartments were separated by means of a proton exchange membrane (Nafion 117, Sigma Aldrich). Both cathodic and anodic compartments were filled with 30 mL of 0.5 M potassium bicarbonate ($KHCO_3$, ACS grade, Sigma-Aldrich, pH≈7.2) electrolyte. Despite the fact that glassy carbon is the most common

Table 1
Different types of catalyst film and GDEs loading by ICP-MS.

Catalyst	Ionomer	Amount of ionomer in the ink (μL)	Theoretical loading ($\mu g_{Au}\ cm_{geo}^{-2}$)	Loading based on ICP-MS analysis ($\mu g_{Au}\ cm_{geo}^{-2}$)	Name in this paper
Unsupported colloidal Au NPs	Nafion	2.6	200	50 ± 1	50 $\mu g_{Au}\ cm_{geo}^{-2}$ Unsupported Au
Unsupported colloidal Au NPs	Nafion	2.6	450	214 ± 12	200 $\mu g_{Au}\ cm_{geo}^{-2}$ Unsupported Au
25 wt% Supported Au/C	–	0	200	143 ± 34	Au/C-No ionomer
25 wt% Supported Au/C	Anion	2.6	200	214 ± 6	Au/C-Low Anion ionomer
25 wt% Supported Au/C	Nafion	2.6	200	210 ± 3	Au/C-Low Nafion ionomer
25 wt% Supported Au/C	Nafion	28.3	200	190 ± 5	Au/C-High Nafion ionomer

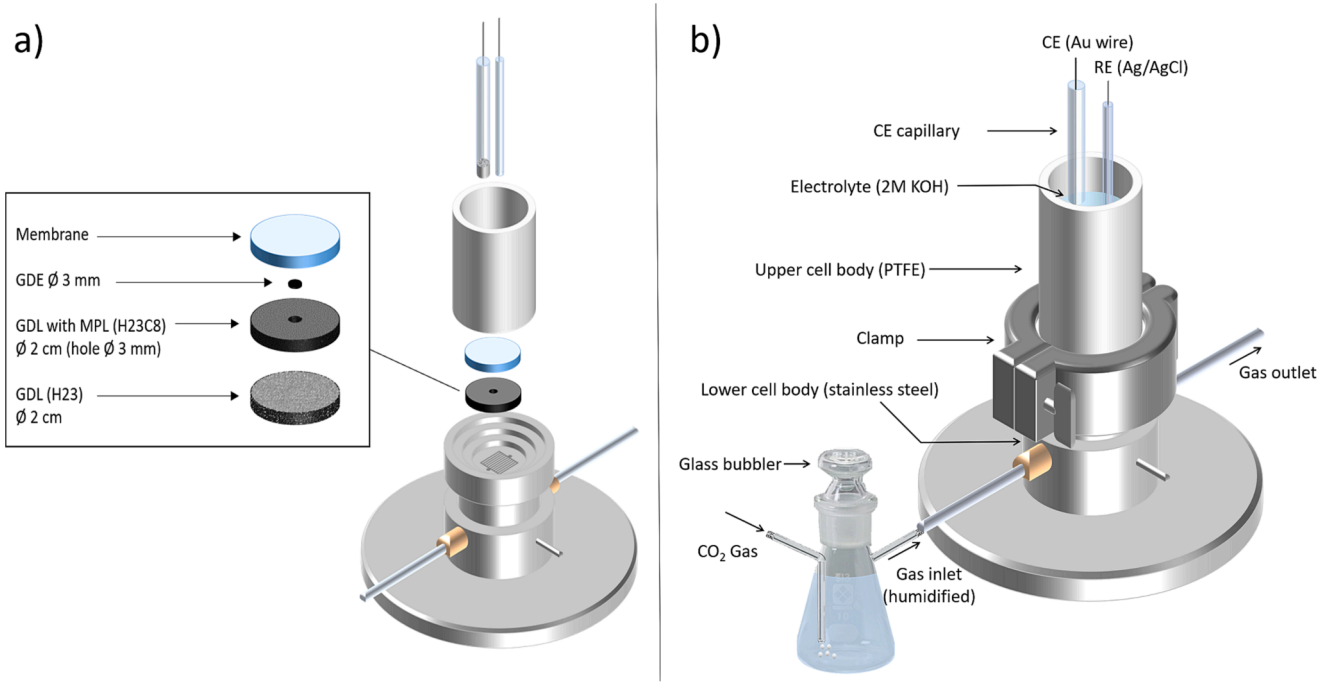

Fig. 2. Sketch of the a) disassembled and b) assembled GDE cell employed in the present study.

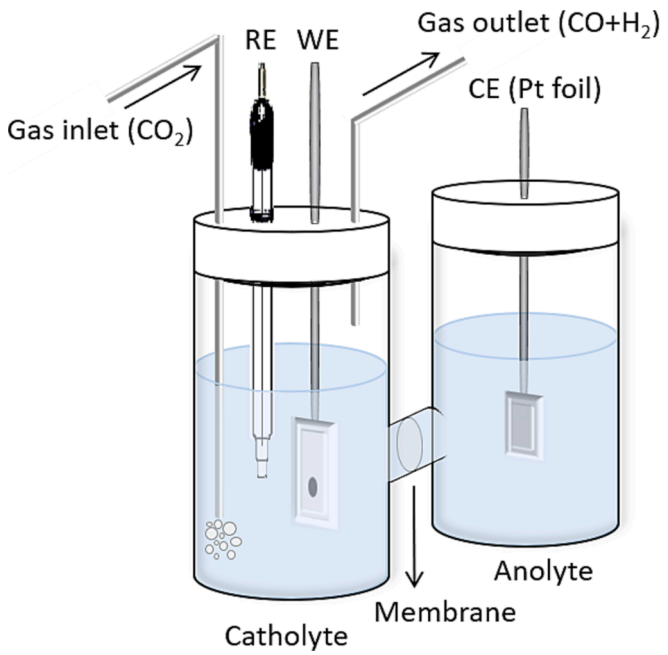

Fig. 3. Sketch of the H-cell employed in the present study.

catalyst substrate in H-cell configurations, to avoid a catalyst substrate effect, we used a GDL as the catalyst substrate in the H-cell setup as in our previous work [26]. This enables a fair comparison between the results of GDE setup and the H-cell setup. For the preparation of the WE for the H-cell, a rectangular piece (0.8 cm × 3 cm) of a GDL with MPL (H23C8, 200 μm thick @ 1 MPa, Freudenberg) was used. The back side and the edges of the electrode were completely covered with Teflon tape in such a manner that only a circular area with diameter of 5 mm remained uncovered. A Ø 5 mm GDE was punched and placed in the aforementioned exposed area. The described WE and a single junction Ag/AgCl (saturated KCl, Pine Research) as a RE were placed in the cathodic compartment. A Pt foil with a dimension of 0.8 cm × 2 cm was placed in the anodic compartment as CE. Prior to the CO_2 electrolysis, both cathodic and anodic compartments were saturated with CO_2 (13 mL min^{-1}) for 30 min. The transport of gaseous products from the headspace of the catholyte to the sample loop of the GC was enabled by a continuous CO_2 flow stream.

2.7. CO_2 electrolysis experiments

Potentiostatic CO_2 electrolysis experiments were carried out for 1 h at selected electrode potentials of −0.4, −0.7, and −1.0 V_{RHE}. Every 10 min the analysis of the gaseous products was carried out by an online gas chromatograph (GC Model 8610C, SRI Instruments) which was triggered by the potentiostat and equipped with a thermal conductivity detector (TCD) and a flame ionization detector (FID) coupled to a methanizer to detect hydrogen and carbon monoxide, respectively. For preventing damages, the column of the GC, the outlet gas of the CO_2RR was passed by a drying tube to remove the excess of water (Cole-Parmer Drierite, Fisher Scientific) before reaching the sample loop of the GC. The gas flow rate was monitored during the CO_2 electrolysis by two flow meters (universal flow meter 7,000 GC by Ellutia) and (Q-Flow 140, FLQ-CTSS-BK-M, CONTREC AG) ensuring that intake and outtake from the cell are identical after setup. We used H_2 (99.999 %), CO_2 (99.999 %), and calibration standard gas from Carbagas (Switzerland) in the electrochemical measurements. For the sake of simplicity and easier comparison between the results of the GDE setup and H-cell measurements, all potentials in this study are converted to the RHE scale based using the following formula $E_{RHE} = E_{Ag/AgCl} + E^0_{Ag/AgCl} + 0.059 \times pH$ (where all potentials are in volts, and $E^0_{Ag/AgCl} = 0.210$ V). The expected pH values based on the concentration of the bulk electrolyte were used for RHE conversions. In the case of using non-concentrated electrolytes in GDE setup, the generation of hydroxide ions from water splitting during high-rate electrolysis will result in a significant change in electrolyte pH which causes the uncertainty of the actual pH at the electrode–electrolyte interface during operating conditions and shows the challenges related to the use of RHE scale [4,11]. Therefore, we changed the electrolyte from 0.5 M $KHCO_3$ in the H-cell to a highly concentrated electrolyte of 2 M KOH in the GDE setup to avoid the local pH deviation.

Moreover, the uncompensated resistance between the WE and RE and the applied electrode potentials were monitored online using an AC signal (5 kHz, 5 mV). In order to realize identical starting conditions for the electrolysis, a fresh WE was used for each experiment. The Faradaic efficiency (FE) for a given gaseous product i was determined based on equation (1):

$$FE_i = \frac{i_i}{i_{total}} = \frac{C_i{*}v{*}z{*}F}{10^6 V_m{*}i_{total}} \quad (1)$$

where i_i (A) represents the partial current for the conversion of CO_2 into product i, i_{total} (A) the total current at the time of the measurement, C_i (Vol%) its concentration measured by on-line GC, ν (L s^{-1}) the gas flow rate, F represents Faraday's constant (96500 C mol^{-1}), z the number of electrons involved in the formation of the particular product, and V_m (L mol^{-1}) the molar volume, which here we consider V_m = 22.4 L mol^{-1} which is the molar volume of an ideal gas at ambient condition. It should be noted that in our GDE setup the small geometric surface area leads to minimal CO_2 consumption and inlet and outlet CO_2 flow are almost identical. For larger surface areas the CO_2 consumption needs to be taken into account when calculating the FE, see Ma et al. [32].

2.8. Inductively coupled plasma-mass spectrometry (ICP-MS)

A Ø 3 circle of freshly prepared catalyst films (GDEs) were placed in a glass test tube. The test tube was kept in a water bath at 60 °C under vigorous stirring. Quickly after adding 5 mL of fresh *aqua regia* into the tube, the tube was closed for 1 h with a help of a stopper. In this way, reaction of the hydrochloric acid (HCl 37 %, Grogg chemie) and nitric acid (HNO_3 65 %, Merk) in a ratio 4:1 in volume could take place inside the tube while the vapor was kept inside it to dissolve the Au NPs embedded on the GDE. The resulted solution was diluted by factors of 100, 50, and 30 with 3 % HNO_3 and was then fed into a NExION 2000 ICP − MS instrument (PerkinElmer) to determine the Au mass loading of the electrodes.

2.9. Small angle X-ray scattering (SAXS) characterization

The data were acquired at Swiss light source. Powder samples were sealed between two 5–7 μm thick mica windows and measurements. The general procedure for SAXS data preparation and measurements follow the approach detailed previously [33]. The measurements were performed directly on NP supported on carbon and a GDL material without Au NPs was used as background. The radially averaged intensity I(q) is given as a function of the scattering vector $q = 4\pi\cdot\sin(\theta)/\lambda$, where λ is the wavelength and 2θ is the scattering angle. The background corrected scattering data were fitted using a power law to take into account the behavior at low q value and a model of polydisperse spheres described by a volume-weighted log-normal distribution. The data were best fitted by adding a second model of polydisperse spheres also described by a volume-weighted log-normal distribution. In most cases this second population is characterized by a large deviation and is probably accounting for the challenges in the background subtraction. In one case, for the sample Au/C- High Nafion ionomer the second population was very pronounced and is believed to actually represent larger size nanoparticles. The scattering data are fitted to the following expression:

$$I(q) = A.q^{-n} + C_1 \int P_{s1}(q,R)V_1(R)D_1(R)dR + C_2 \int P_{s2}(q,R)V_2(R)D_2(R)dR$$

where $A\cdot q^{-n}$ corresponds to the power law while A and n are free parameters; C_1 and C_2 are scaling constants, P_{s1} and P_{s2} the sphere form factor, V_1 and V_2 the particle volumes, D_1 and D_2 the log-normal size distributions. The sphere form factor is given by:

$$Ps(q,R) = \left(3\frac{\sin(qR) - qR\cos(qR)}{(qR)^3}\right)^2$$

and the log-normal distribution by:

$$D(R) = \frac{1}{R\sigma\sqrt{2\pi}}\exp\left(\frac{-\left[\ln\left(\frac{R}{R0}\right)\right]^2}{2\sigma^2}\right)$$

where σ is the variance and R_0 the geometric mean of the log-normal distribution.

The fitting was done using home written MATLAB code to optimize agreement between data and model available upon request. The free parameters in the model are: A, n, R_1, R_2, C_1, C_2, σ_1, σ_2, C_1 and C_2. The values obtained for these parameters are reported in Table S2 with the corresponding fits in Fig. S7.

The average volume of nanoparticle from population 1 and from population 2, $<V>_1$ and $<V>_2$ respectively, lead to define volume fraction of population 1, Φ_{V1}, and volume fraction of population 2, Φ_{V2}, as:

$$\Phi_{V1} = \frac{N_1 < V >_1}{N_1 < V >_1 + N_2 < V >_2} = 1 - \Phi_{V2}$$

$$\frac{\Phi_{V1}}{\Phi_{V2}} = \frac{N_1 < V >_1}{N_2 < V >_2}$$

$$\frac{N_1}{N_2} = \frac{\Phi_{V1} < V >_2}{\Phi_{V2} < V >_1}$$

where N_1 and N_2 are the number of nanoparticles in the population 1 or 2 respectively.

From the SAXS data acquisition we have the relationship between the retrieved coefficient C_1 and C_2 given by $C_i = k.\ \Phi_{vi}.\ <V>_i$ where i = 1 or 2 and k is a constant.

$$k = \frac{C_1}{\Phi_{V1} < V >_1} = \frac{C_2}{\Phi_{V2} < V >_2} = \frac{C_2}{(1 - \Phi_{V1}) < V >_2}$$

$$\frac{\Phi_{V1}}{1 - \Phi_{V1}} = \frac{C_1 < V >_2}{C_2 < V >_1}$$

$$\Phi_{V1} = \frac{1}{1 + \frac{C_2 <V>_1}{C_1 <V>_2}}$$

In order to weight the probability density function by the area or surface fractions we consider $<A>_1$ and $<A>_2$ as the average area of the nanoparticles from population 1 and 2, respectively:

$$\Phi_{A1} = \frac{N_1\langle A\rangle_1}{N_1\langle A\rangle_1 + N_2\langle A\rangle_2} = 1 - \Phi_{A2} = \frac{1}{1 + \frac{N_2\langle A\rangle_2}{N_1\langle A\rangle_1}}$$

$$\Phi_{A1} = \frac{1}{1 + \frac{\Phi_{V2}\langle A\rangle_1\langle A\rangle_2}{\Phi_{V1}\langle A\rangle_2\langle A\rangle_1}}$$

$$\Phi_{A1} = \frac{1}{1 + \frac{C_2\ (\langle V\rangle_1)^2\langle A\rangle_2}{C_1\ (\langle V\rangle_2)^2\langle A\rangle_1}}$$

2.10. Contact angle analysis

Contact angle measurements were performed on a Krüss Advance Drop Shape Analyzer DSA25 (Krüss GmbH, Hamburg, Germany). Electrodes were mounted on a flat stage with the catalyst layer face-up. Sessile water drops (Milli-Q water) of 1.4 μL were deposited at room temperature and the image was captured by the equipped CCD camera.

3. Result and discussion

In the following we discuss the influence of different factors that are relevant for an optimization of the CO_2RR performance in a GDE with zero-gap design. Previous investigations, which involved the analysis of

both pristine and used catalyst particles using identical location scanning electron microscopy (IL-SEM), indicated that the decline in CO selectivity observed in the GDE setup utilizing an Ag-based catalyst cannot be attributed solely to the active phase of the catalyst. Potential catalyst issues, such as particle agglomeration or structural changes in the Ag NPs, were ruled out. Instead, the deterioration in selectivity was linked to the degradation of the catalyst layer [27]. It was postulated that porosity plays a pivotal role in preventing performance degradation associated with flooding [28]. Furthermore, factors such as the ionomer to catalyst ratio have been shown to have substantial influence on the selectivity towards CO [34].

In this study, which extends the pursuit of optimizing zero-gap design GDEs, we employed Au NPs as the catalyst, a standard choice known for its high FE towards CO.

3.1. Factors influencing the decay in FE with time

To investigate the impact of membrane selection on the selectivity and activity of the Au catalyst, we initially compared two membrane types: an anion exchange membrane and a Nafion membrane. We conducted 1-hour CO_2 electrolysis experiments with an unsupported Au catalyst, both loaded with 50 μg_{Au} cm_{geo}^{-2}, using these two different membrane types within the GDE setup. The results are presented in Fig. 4. Please note that all uncertainties (represented by error bars) in this study are based on the standard deviation from three independent measurements, as detailed in Table S1.

To isolate the membrane's influence, we kept all other parameters constant. As shown in Fig. 4, during the initial stages of the CO_2 electrolysis experiment, the use of a Nafion membrane led to a slightly higher selectivity (FE_{CO}) towards CO. However, both membranes exhibited a degradation in CO selectivity over time. Notably, with the anion exchange membrane, the absolute reaction rate at the beginning of the electrolysis (150 mA cm_{geo}^{-2}) was approximately 50 % higher than when using a Nafion membrane (100 mA cm_{geo}^{-2}). Analyzing the absolute reaction rates, we observed that the decline in selectivity stemmed from a decrease in the absolute CO current density (i.e., the current associated with carbon monoxide production) over time, while the H_2 current density remained relatively stable throughout the experiments. Considering that both absolute CO and H_2 current densities were significantly higher when employing the anion exchange membrane, we conclude that this membrane type provides a more favorable reaction environment for the CO_2RR. Consequently, for all subsequent measurements in this study, we employed the anion exchange membrane in our "zero-gap design" GDE setup.

To ascertain whether the decline in CO selectivity observed over time is attributed to insufficient humidification within the GDE configuration, we conducted the following experiment: Following a 1-hour CO_2 electrolysis using an unsupported Au catalyst loaded at 50 μg_{Au} cm_{geo}^{-2} and operated at −0.7 V_{RHE} E, the system was maintained at the open circuit potential (OCP) for 30 min. During this 30-minute interval, humidified CO_2 was consistently purged beneath the catalyst layer. Subsequently, another 1-hour CO_2 electrolysis at −0.7 V_{RHE} was performed, as illustrated in Fig. 5. The results clearly demonstrate that the selectivity performance did not show improvement even after maintaining the system at OCP while continuously purging it with humidified CO_2. This suggests that the diminishing selectivity towards CO observed within the GDE setup is not attributable to a deficiency in humidification.

In the following analysis, we explored three potential origins for the observed degradation of the catalyst layer over time: i) membrane instability, ii) the catalyst layer substrate (the GDL), and iii) the degradation of the Au NPs. We examined each of these factors to assess their impact on the declining performance.

To investigate the potential influence of membrane instability during CO_2 electrolysis, we conducted a 1-hour experiment using an unsupported Au catalyst loaded at 50 μg_{Au} cm_{geo}^{-2}, as depicted in Fig. 6-a. Following this experiment, we introduced a new membrane into the cell while keeping the same WE, as illustrated in Fig. 6-b. It's noteworthy that we observed no discernible improvement in either activity or selectivity. Consequently, we concluded that the degradation primarily emanates from the catalyst layer and is not attributed to membrane degradation. In our prior study [26], we further substantiated this by subjecting a blank GDL (H23C8) to a 1-hour CO_2 electrolysis at −0.7 V_{RHE}. This was undertaken to confirm that the catalyst substrate was not the source of the degradation and to establish that the GDL remained unaltered at this applied potential, thereby ruling out the GDL as the source of CO production.

In addition to the aforementioned tests, we conducted an additional

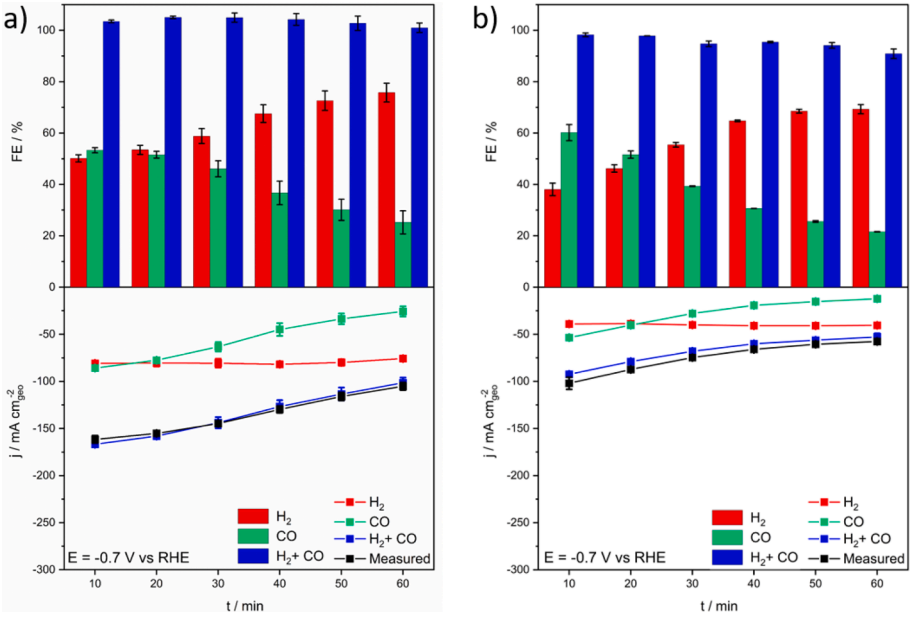

Fig. 4. FEs and current densities of the gaseous products obtained from CO_2RR on 50 μg_{Au} cm_{geo}^{-2} of unsupported Au catalyst with a fresh a) anion exchange, and b) Nafion membrane, every 10 min of 1-hour CO_2 electrolysis at −0.7 V_{RHE} in GDE setup. All indicated uncertainties are the standard deviation from three independent measurements.

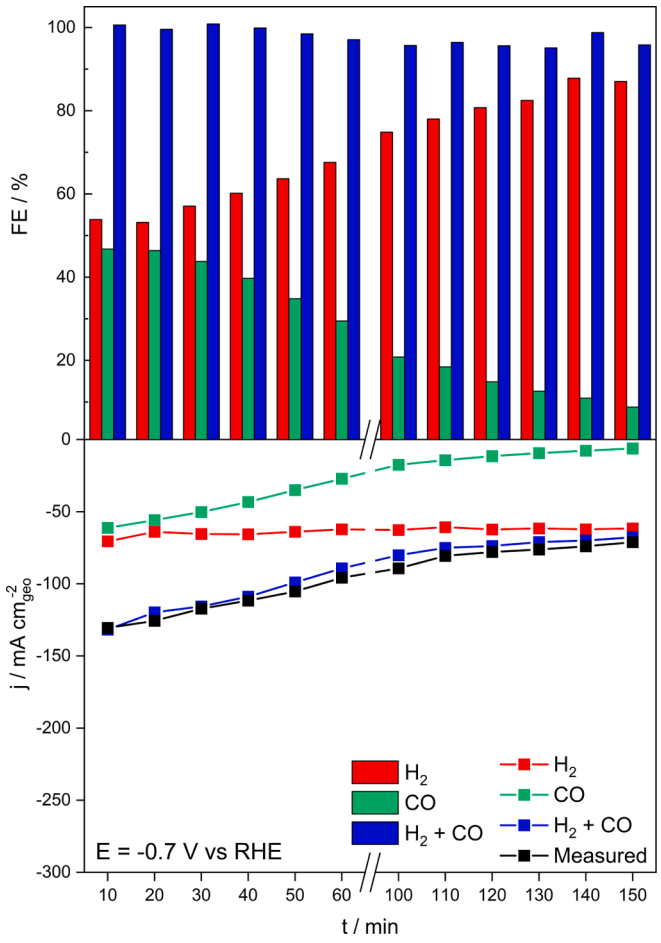

Fig. 5. FEs and current densities of the gaseous products obtained from CO_2RR on 50 μg_{Au} cm^{-2}_{geo} of unsupported Au catalyst every 10 min of 2 rounds of 1-hour CO_2 electrolysis at −0.7 V_{RHE} with an interval of 30 min at OCP, in GDE setup.

experiment aimed at probing the potential influence of the membrane. In Fig. 7-b, we present the FE_{CO} and current densities obtained from a 1-hour CO_2 electrolysis at −0.7 V_{RHE} within the Gas-Diffusion Electrode (GDE) setup employing a 50 μg_{Au} cm^{-2}_{geo} unsupported Au catalyst. In this setup, we introduced 5 μL of 0.5 M $KHCO_3$ between the catalyst film and the anion exchange membrane.

Notably, our findings reveal an enhancement in FE_{CO} when a solid-supported electrolyte layer is introduced adjacent to the catalyst film. This observation aligns with the findings of Li et al. [5] and Salvatore et al. [6]. Despite this promising improvement, we refrained from consistently using KHCO3 drop-casting on the catalyst layer for the remaining experiments. The decision stemmed from the inherent challenge in preparing the cell in the presence of $KHCO_3$, which risked rendering the cell assembly procedure irreproducible, thereby limiting the valuable insights gained from utilizing the GDE setup.

While the work of Salvatore et al. [6] suggests that incorporating a solid-supported aqueous electrolyte layer may be crucial for achieving high CO selectivity, the precise role of this layer remains elusive. These researchers have also demonstrated that by replacing the solid-supported aqueous $NaHCO_3$ layer with a solid-supported water layer, FE_{CO} remained consistent at all current density values up to 200 mA cm^{-2}_{geo} in their GDE setup [6]. We confirmed this observation in our GDE setup by substituting 5 μL of 0.5 M $KHCO_3$ with water, without fully drying the anion exchange membrane before incorporating it into the setup. Our results revealed that replacing KHCO3 with water did not alter FE_{CO}, as shown in Fig. 7-c. This outcome suggests that it is not $KHCO_3$, but rather water, that plays a pivotal role in the performance of the solid support layer.

It is important to note that in all three cases, whether using a dried anion exchange membrane (Fig. 7-a), a dried anion exchange membrane with 5 μL of 0.5 M $KHCO_3$ added between the catalyst and anion exchange membrane (Fig. 7-b), or applying a wet anion exchange membrane (Fig. 7-c), the total current density remained relatively constant. In all measurements, we consistently achieved an initial value of approximately 150 mA mA cm^{-2}_{geo}. Additionally, as shown in Fig. S1 for the same experiments conducted over an extended duration of CO_2 electrolysis (2 h), the selectivity improvements observed in the GDE setup were temporary and did not endure beyond a limited timeframe.

In the subsequent phase of this work, we increased the loading of the GDE film from 50 μg_{Au} cm^{-2}_{geo} of unsupported Au catalyst to 200 μg_{Au}

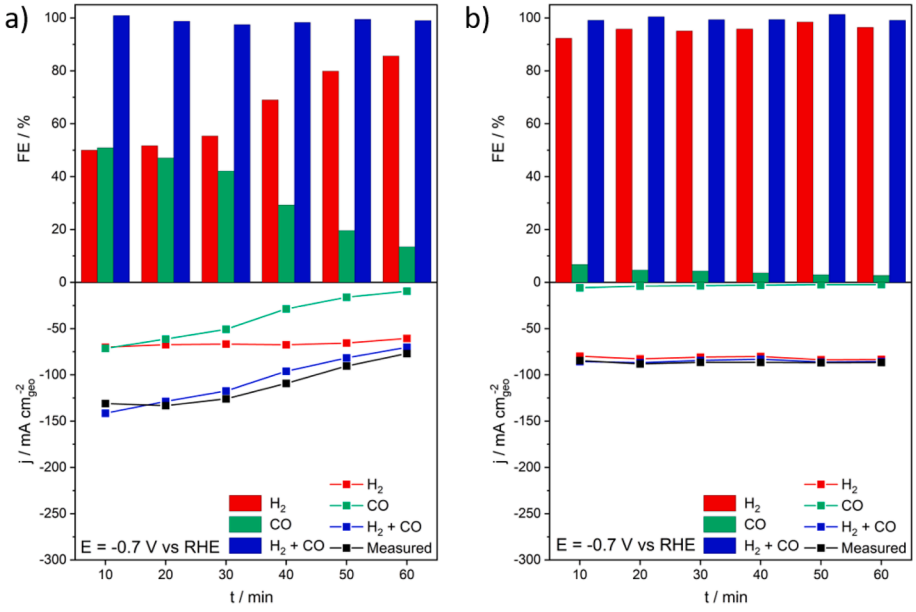

Fig. 6. FEs and current densities of the gaseous products obtained from CO_2RR on 50 μg_{Au} cm^{-2}_{geo} of a) unsupported Au catalyst with an Anion exchange membrane, b) same Au catalyst with a new fresh Anion exchange membrane every 10 min of 1-hour CO_2 electrolysis at −0.7 V_{RHE} in GDE setup.

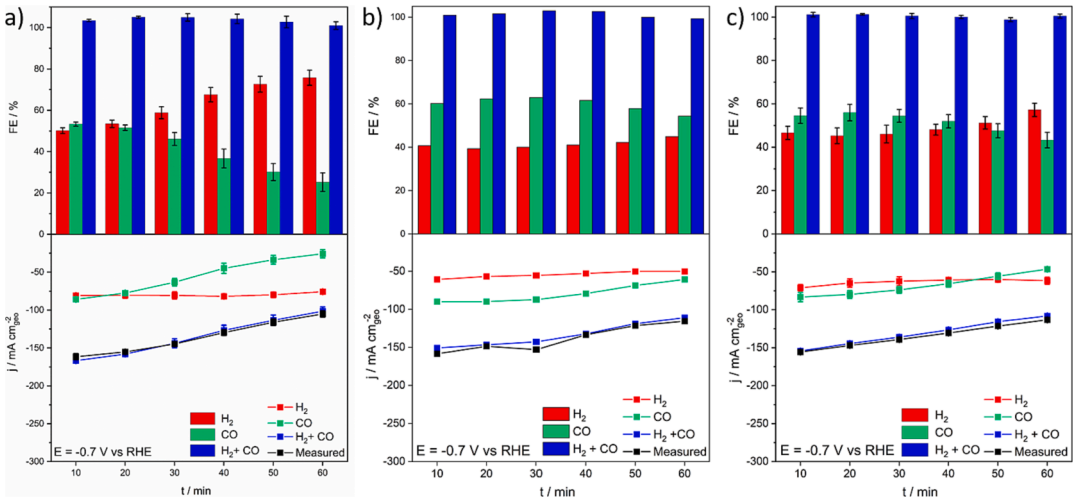

Fig. 7. FEs and current densities of the gaseous products obtained from CO_2RR on 50 μg_{Au} cm^{-2}_{geo} of unsupported Au catalyst with a fresh a) dried anion exchange membrane (data taken from ref. [26]), b) dried anion exchange membrane with 5 µL of 0.5 M $KHCO_3$ between the catalyst and anion exchange membrane, and c) wet anion exchange membrane, every 10 min of 1-hour CO_2 electrolysis at −0.7 V_{RHE}, in GDE setup. All indicated uncertainties are the standard deviation from three independent measurements.

cm^{-2}_{geo}. We then conducted 1-hour CO_2 electrolysis experiments in both the GDE setup, as depicted in Fig. 8, and the H-cell configuration, showcased in Fig. 9. Surprisingly, in both experimental setups, increasing the metal loading did not yield a substantial increase in absolute current density. This observation strongly suggests that there may be incomplete utilization of the catalyst layer. In fact, in the GDE setup, we even noted a decline in current densities. This phenomenon implies that the heightened metal loading restricts the accessibility of unsupported Au NPs, likely due to the formation of a denser and less porous catalyst layer. However, despite the absence of significant improvements in current densities, there was a noticeable enhancement in the selectivity toward CO production in both experimental setups. This intriguing result suggests that the increase in metal loading, while not leading to higher current densities, has a positive impact on the selective generation of CO.

3.2. *Benefits of supported Au NPs and the effect of ionomer on supported catalysts*

The findings presented above clearly underscore the limitations inherent in unsupported catalyst layers, particularly regarding the accessibility of active sites. In order to achieve high current densities, it is imperative to prepare catalyst layers on GDLs so that are more accessible. As previously mentioned, porosity plays a pivotal role in mitigating performance losses associated with flooding [28]. Consequently, we opted to anchor the Au NPs onto a porous, high-surface-area carbon substrate, employing a strategy reminiscent of those explored in fuel cell technology approximately three decades ago [35]. This approach not only curbs NP agglomeration but also provides the catalyst layer with a porous structure that benefits reactants and products alike. Importantly, we maintained the same quantity of ionomer binder in the ink as was used for the unsupported Au catalyst, resulting in a low

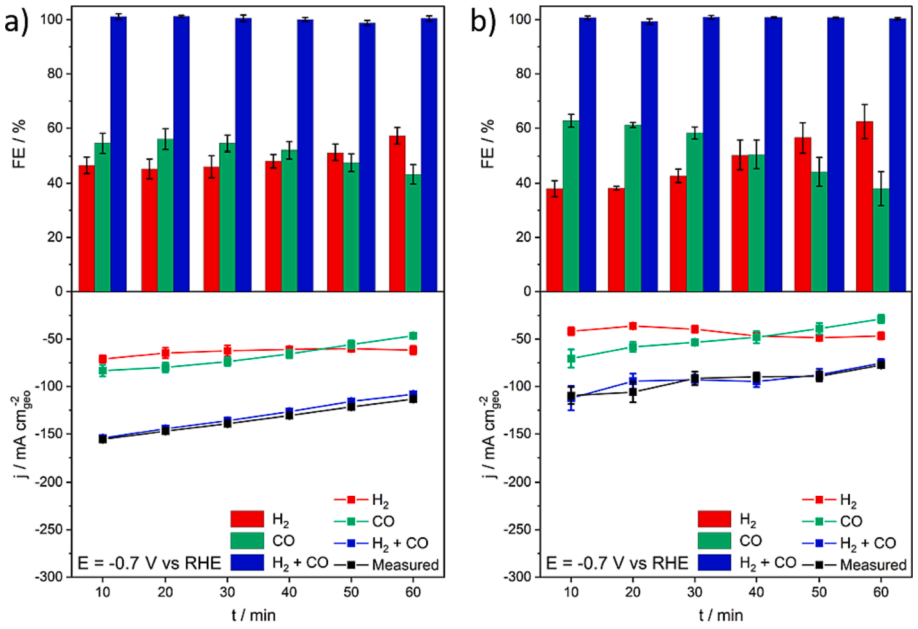

Fig. 8. FEs and current densities of the gaseous products obtained from CO_2RR on a) 50 μg_{Au} cm^{-2}_{geo} and b) 200 μg_{Au} cm^{-2}_{geo} of unsupported Au catalyst, every 10 min of 1-hour CO_2 electrolysis at −0.7 V_{RHE}, in GDE setup. All indicated uncertainties are the standard deviation from three independent measurements.

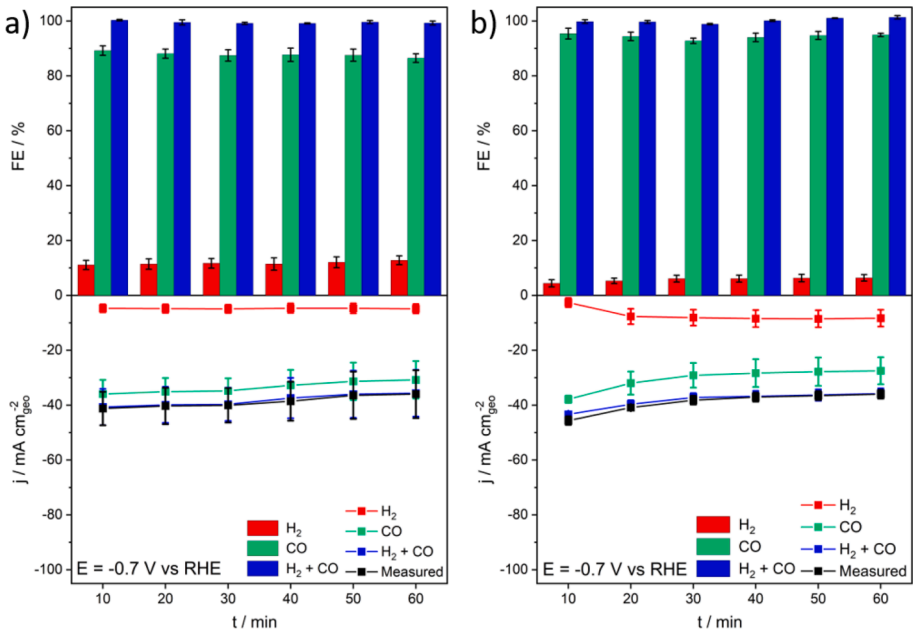

Fig. 9. FEs and current densities of the gaseous products obtained from CO_2RR on a) 50 μg_{Au} cm^{-2}_{geo} and b) 200 μg_{Au} cm^{-2}_{geo} of unsupported Au catalyst, every 10 min of 1-hour CO_2 electrolysis at −0.7 V_{RHE}, in H-cell configuration. All indicated uncertainties are the standard deviation from three independent measurements.

Nafion ionomer content.

The outcome of supporting the Au NPs on carbon was a marked increase in absolute reaction rates, as illustrated in Fig. 10-a. This transformation not only rendered the catalyst layer more active but also reduced the favorability of the hydrogen evolution reaction (HER). These results signify that the support of Au NPs on carbon significantly enhanced the accessibility of the particles for the chemical reactions. Carbon, with its expansive specific surface area, high porosity, and superb electron conductivity, plays a pivotal role as a catalyst support. To delve deeper into the supporting effect, we varied the ionomer content in the ink formulation. This variation encompassed a high ionomer content (Au/C- High Nafion ionomer), an absence of ionomer (Au/C- No ionomer), and replacement of the ionomer with an anion exchange ionomer (Au/C- Low Anion ionomer), as depicted in Fig. 10-b, Fig. 10-c, and Fig. 10-d, respectively.

It is evident that increasing the Nafion ionomer content resulted in a less active catalyst layer, leading to a decrease in total current density from 250 to 150 mA cm^{-2}_{geo}. Simultaneously, the parasitic HER gained prominence, with its FE increasing from 5 % to 30 % at the outset of the CO_2 electrolysis. In contrast, in cases where ionomer was absent (Fig. 10-c) or replaced with an anion exchange ionomer (Fig. 10-d), the FE of the HER surged to around 80 %. However, these alterations were accompanied by a substantial reduction in total current density to approximately 100 mA cm^{-2}_{geo}. Notably, samples lacking ionomer exhibited higher cell resistance (approximately 45 Ω) compared to samples with ionomer (around 20 Ω), underscoring the poor ionic conductivity of the catalyst film in the absence of ionomer. For the sake of comprehensiveness, Figs. S2-S5 present the CO_2 electrolysis on supported Au/C with different ionomer contents in the GDE setup, spanning different applied potentials (−0.4, −0.7, and −1 VRHE). These supplementary figures corroborate the generality of our observations.

The corresponding experiments conducted in the H-cell setup are depicted in Fig. S6. In contrast to the results observed in the GDE measurements, altering the ionomer content in the H-cell setup led to a

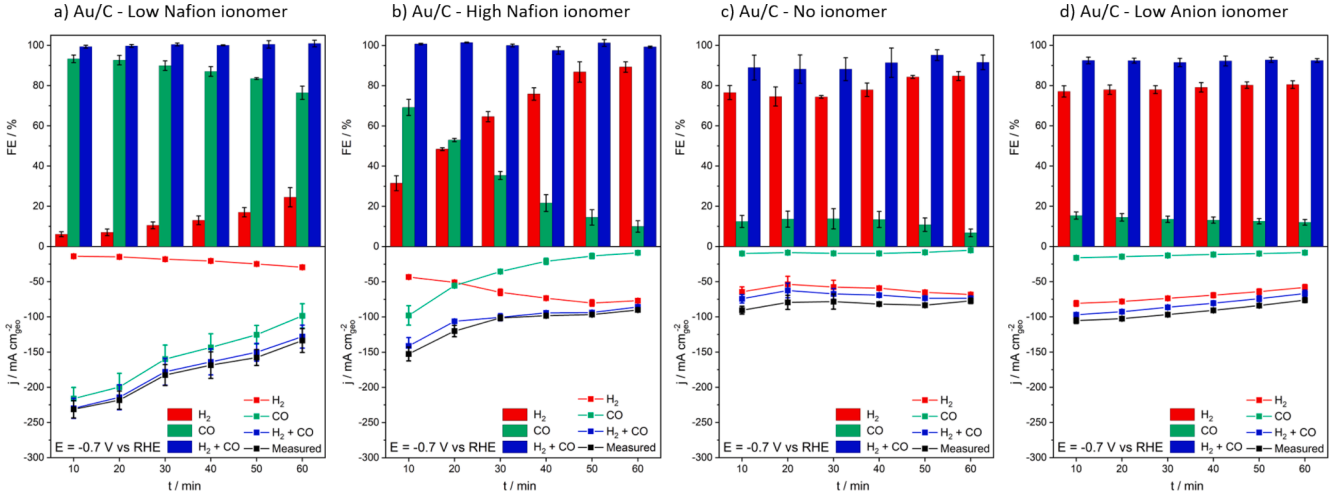

Fig. 10. FEs and current densities of the gaseous products obtained from CO_2RR on supported Au/C catalyst with a) low Nafion ionomer, b) high Nafion ionomer, c) no ionomer, and d) low Anion ionomer every 10 min of 1-hour CO_2 electrolysis at −0.7 V_{RHE}, in GDE setup. All indicated uncertainties are the standard deviation from three independent measurements.

slight increase in the total current density, rising from 55 to 70 mA cm^{-2}_{geo}, without any discernible impact on the HER FE. In line with the GDE measurements, the total current density significantly dropped to approximately 25 mA cm^{-2}_{geo} when no ionomer was used, concurrently with an increase in the HER FE to 37 %. Notably, substituting Nafion with an anion exchange ionomer did not result in substantial changes in catalyst performance. These findings emphasize the critical role of realistic reaction conditions in catalyst screening methods, such as those provided by the GDE setup. In a GDE setup, we clearly observe the influence of the ionomer used, whereas this influence is not as pronounced in an H-cell setup.

To further illustrate the intricate effects of ionomers, we conducted contact angle measurements, as illustrated in Fig. 11. It is worth noting that while electrolysis conditions can induce electrocapillary forces, which can alter the surface contact angle under electric bias [36], the electroless contact angle can still offer insights into the wetting behavior of the catalyst layers [37]. Based on the surface contact angle results and assuming equal roughness (hydrophobicity and surface roughness jointly determine the surface contact angle), we observed that supported Au/C catalyst layers tend to be more hydrophobic than unsupported catalyst layers. The GDL used, with its microporous carbon layer, exhibits high hydrophobicity. However, depositing the catalyst in the form of a metal layer renders the surface more hydrophilic, aligning with the typical hydrophilicity of metal surfaces. Interestingly, when supporting the catalyst layer, the hydrophobic properties of the carbon support appear to dominate the wettability. The results indicate that the quantity of Nafion used in the layer does not significantly influence this wettability. Nonetheless, in cases where no ionomer is employed in the catalyst layer, the surface exhibits hydrophilic behavior. Furthermore, an anion exchange ionomer renders the surface more hydrophilic than the Nafion ionomer. Hence, the lower performance observed in the unsupported Au catalyst, as well as in the supported Au/C catalyst with no ionomer and low anion ionomer samples, may be at least partially attributed to the highly hydrophilic nature of the surface of these samples, which could potentially lead to flooding of the catalyst layer [37].

Finally, we conducted an ex situ SAXS analysis to investigate the different catalyst layers and examine the potential agglomeration of Au NPs. SAXS, as an integrative method, provides more comprehensive insights into the entire layer compared to IL-SEM, which is a local method. The SAXS analyses revealed that the average particle size of supported Au/C NPs (9.2 ± 2.1 nm) is slightly larger than that of unsupported Au NPs (8.6 ± 1.7 nm), indicating minute agglomeration upon supporting, as detailed in Table S2 and illustrated in Fig. S7. Remarkably, while the particle size of unsupported Au NPs remained constant after electrolysis, a noticeable increase in the average particle size, from 8.2 ± nm to 11.0 ± nm, was observed for the Au/C catalyst, as also documented in Table S2 and Fig. S8. This observation appears to align with the results from the electrolysis measurements, where a decrease in total current density was noted for the Au/C catalyst, Fig. 10-a, whereas the total current density of the unsupported Au NPs remained stable, Fig. 8-b. However, it's crucial to note that, even with this increase in particle size, the Au/C catalysts still deliver six times more current density than unsupported Au NPs at the same applied potential.

Interestingly, the augmentation in particle size under electrolysis conditions seems to be contingent on the ionomer content in the catalyst layer. In the presence of Nafion ionomer, a size increase is observed for both low and high ionomer content, while the average particle size remains relatively constant when an anion exchange ionomer is used, as demonstrated in Fig. S9 and Table 2. This implies that an increase in Nafion content within the catalyst layer leads to heightened agglomeration during electrochemical tests. Table 2 highlights that while a relatively minor increase in the average particle size, from around 8 nm to approximately 12 nm, occurs for Au/C with low Nafion ionomer content, high Nafion ionomer content in the Au/C catalyst layer results in the formation of larger Au NPs. After the electrolysis, the average particle size increases from around 8 nm to over 20 nm. This significant particle agglomeration at high Nafion content is attributed to local pH effects. In cases of low Nafion content, the local pH is offset by the increased current density (of the supported NPs), facilitating the transport of more protons to the cathode. Conversely, when the Nafion content is excessive, the current density decreases, diminishing the potential for pH regulation.

Notably, the trends observed in the loss of absolute current density during electrolysis, as depicted in Fig. 10, do not precisely mirror the reduction in surface area. Surprisingly, the relative loss in absolute current density is even more pronounced in the case of low Nafion ionomer content, despite the minor particle agglomeration. This suggests that while particle agglomeration does occur, it may not be the primary driver behind the decline in absolute current density. On the contrary, the results indicate that the complete surface area of the Au NPs is still not fully utilized, as otherwise, a more significant impact from the observed agglomeration would be anticipated.

4. Conclusion

In this comprehensive study, we examined the key parameters crucial for optimizing the CO_2RR performance of an Au catalyst layer within a zero-gap GDE setup. It's important to note that the insights gained using the zero-gap GDE setup diverge from what one might deduce from investigations conducted within an H-cell setup. Our results, presented here, reveal that in the GDE setup, the use of anion exchange membranes leads to achieving higher current densities for the

Table 2
The average Au NPs diameter based on SAXS analysis.

	Before CO_2 electrolysis [nm]	After CO_2 electrolysis [nm]
Au NPs- Low Nafion ionomer	8.6 ± 1.7	8.2 ± 1.6
Au/C- Low Nafion ionomer	9.2 ± 2.1	12.1 ± 4.4
Au/C- High Nafion ionomer	7.8 ± 2.2	20.7 ± 8.6
Au/C- Low Anion ionomer	12.1 ± 3.7	11.7 ± 3.4

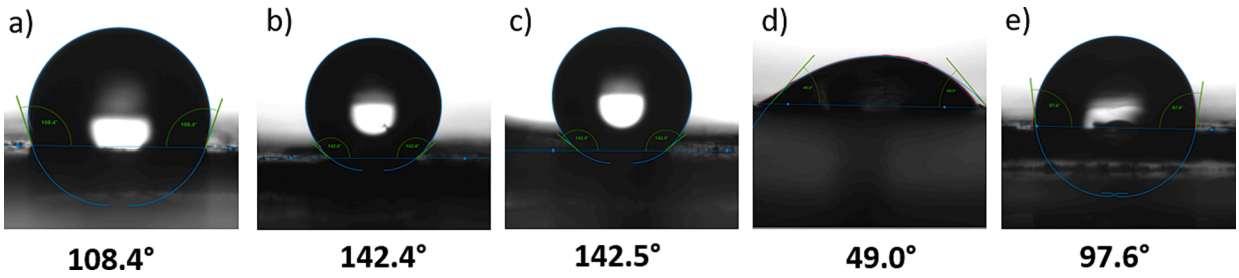

Fig. 11. The surface contact angle images of as prepared a) unsupported Au NPs with low Nafion ionomer, and supported Au/C catalyst with b) low Nafion ionomer, c) high Nafion ionomer, d) no ionomer, and e) low Anion ionomer on GDL, before performing CO_2 electrolysis.

same catalyst in comparison to Nafion exchange membranes. Intriguingly, this preference for anion exchange membranes does not extend to the choice of binder in the catalyst layer, where Nafion proved to be more favorable for performance. Crucially, our study demonstrates that supported Au NPs result in significantly higher current densities when compared to unsupported counterparts, notwithstanding the potential for agglomeration during the supporting process. This underscores the vital role of porosity, akin to fuel cell catalyst layers, in ensuring complete utilization. Nevertheless, working with supported catalysts introduces its own set of challenges, including susceptibility to agglomeration. While the average particle size remains relatively stable during electrolysis with an unsupported NP layer, our SAXS analysis indicates a size increase for supported Au NPs.

Moreover, our findings highlight the necessity for optimizing the Nafion ionomer content within the catalyst layer when employing supported Au NPs. This optimization is contingent upon the specific catalyst type and ideally should be tailored for each unique catalyst, with the "zero-gap GDE design" offering a straightforward and efficient approach. Notably, our studies reveal that the extent of particle agglomeration is linked to the type and quantity of ionomer in the catalyst layer. High Nafion content, in particular, leads to substantial particle agglomeration. While the exact reasons behind this observation are subject to speculation, it's plausible that ionomer-dependent particle growth may be influenced by variations in local pH.

Lastly, despite the observation of particle agglomeration, there is no direct correlation with the observed decline in absolute reaction rate. Hence, we infer that another mechanism is at play, responsible for the observed degradation in performance over time, affecting both the absolute reaction rate and FE. Similar to conclusions drawn for supported Ag NPs [25,26], we posit that, in the case of Au NPs in a zero-gap configuration, the formation of bicarbonate precipitates is the primary contributor to the observed performance decay. Even the porosity introduced by supporting Au NPs appears insufficient to mitigate this issue, potentially exacerbated by higher current densities associated with supported NPs, leading to enhanced precipitate formation.

5. Declaration of Generative AI and AI-assisted technologies in the writing process

During the preparation of this work the authors used ChatGPT to review individual sections of the manuscript to improve the readability and style of the text. After using ChatGPT, the authors reviewed and edited the content as needed and take full responsibility for the content of the publication. No references were included based on the use of ChatGPT.

Declaration of Competing Interest

The authors declare that they have no known competing financial interests or personal relationships that could have appeared to influence the work reported in this paper.

Data availability

Data will be made available on request.

Acknowledgment

This work was supported by the Swiss National Science Foundation (SNSF) via the project No. 200021_184742. The Niels Bohr Institute, University of Copenhagen, Denmark, is thanked for access to SAXS equipment, in particular J. K. K. Kirkensgaard.

Appendix A. Supplementary material

Supplementary data to this article can be found online at https://doi.org/10.1016/j.jcat.2023.115209.

References

[1] J. Oerlemans, Atmospheric science: Extracting a climate signal from 169 glacier records, Science (80-.) 308 (2005) 675–677, https://doi.org/10.1126/science.1107046.
[2] H.R.M. Jhong, S. Ma, P.J. Kenis, Electrochemical conversion of CO2 to useful chemicals: Current status, remaining challenges, and future opportunities, Curr. Opin. Chem. Eng. 2 (2013) 191–199, https://doi.org/10.1016/j.coche.2013.03.005.
[3] S. Verma, B. Kim, H.R.M. Jhong, S. Ma, P.J.A. Kenis, A gross-margin model for defining technoeconomic benchmarks in the electroreduction of CO2, ChemSusChem. 9 (2016) 1972–1979, https://doi.org/10.1002/cssc.201600394.
[4] T. Burdyny, W.A. Smith, CO2 reduction on gas-diffusion electrodes and why catalytic performance must be assessed at commercially-relevant conditions, Energy Environ. Sci. 12 (2019) 1442–1453, https://doi.org/10.1039/c8ee03134g.
[5] Y.C. Li, D. Zhou, Z. Yan, R.H. Gonçalves, D.A. Salvatore, C.P. Berlinguette, T. E. Mallouk, Electrolysis of CO2 to Syngas in Bipolar Membrane-Based Electrochemical Cells, ACS Energy Lett. 1 (2016) 1149–1153, https://doi.org/10.1021/acsenergylett.6b00475.
[6] D.A. Salvatore, D.M. Weekes, J. He, K.E. Dettelbach, Y.C. Li, T.E. Mallouk, C. P. Berlinguette, Electrolysis of Gaseous CO2 to CO in a Flow Cell with a Bipolar Membrane, ACS Energy Lett. 3 (2018) 149–154, https://doi.org/10.1021/acsenergylett.7b01017.
[7] B. Endrődi, G. Bencsik, F. Darvas, R. Jones, K. Rajeshwar, C. Janáky, Continuous-flow electroreduction of carbon dioxide, Prog. Energy Combust. Sci. 62 (2017) 133–154, https://doi.org/10.1016/j.pecs.2017.05.005.
[8] D.M. Weekes, D.A. Salvatore, A. Reyes, A. Huang, C.P. Berlinguette, Electrolytic CO2 Reduction in a Flow Cell, Acc. Chem. Res. 51 (2018) 910–918, https://doi.org/10.1021/acs.accounts.8b00010.
[9] C.M. Gabardo, A. Seifitokaldani, J.P. Edwards, C.T. Dinh, T. Burdyny, M.G. Kibria, C.P. O'Brien, E.H. Sargent, D. Sinton, Combined high alkalinity and pressurization enable efficient CO2 electroreduction to CO, Energy Environ. Sci. 11 (2018) 2531–2539, https://doi.org/10.1039/c8ee01684d.
[10] S. Ma, R. Luo, J.I. Gold, A.Z. Yu, B. Kim, P.J.A. Kenis, Carbon nanotube containing Ag catalyst layers for efficient and selective reduction of carbon dioxide, J. Mater. Chem. a. 4 (2016) 8573–8578, https://doi.org/10.1039/c6ta00427j.
[11] J.J. Lv, M. Jouny, W. Luc, W. Zhu, J.J. Zhu, F. Jiao, A Highly Porous Copper Electrocatalyst for Carbon Dioxide Reduction, Adv. Mater. 30 (2018) 1–8, https://doi.org/10.1002/adma.201803111.
[12] I. Merino-Garcia, E. Alvarez-Guerra, J. Albo, A. Irabien, Electrochemical membrane reactors for the utilisation of carbon dioxide, Chem. Eng. J. 305 (2016) 104–120, https://doi.org/10.1016/j.cej.2016.05.032.
[13] W. Lee, Y.E. Kim, M.H. Youn, S.K. Jeong, K.T. Park, Catholyte-Free Electrocatalytic CO2 Reduction to Formate, Angew. Chemie - Int. Ed. 57 (2018) 6883–6887, https://doi.org/10.1002/anie.201803501.
[14] R.B. Kutz, Q. Chen, H. Yang, S.D. Sajjad, Z. Liu, I.R. Masel, Sustainion Imidazolium-Functionalized Polymers for Carbon Dioxide Electrolysis, Energy Technol. 5 (2017) 929–936, https://doi.org/10.1002/ente.201600636.
[15] A.A. Samu, A. Kormányos, E. Kecsenovity, N. Szilágyi, C. Janáky, Intermittent Operation of CO 2 Electrolyzers at Industrially Relevant Current Densities, Cite This ACS Energy Lett. 2022 (2022) 1859–1861, https://doi.org/10.1021/acsenergylett.2c00923.
[16] T.N. Nguyen, C.T. Dinh, Gas diffusion electrode design for electrochemical carbon dioxide reduction, Chem. Soc. Rev. 49 (2020) 7488–7504, https://doi.org/10.1039/d0cs00230e.
[17] D. Higgins, C. Hahn, C. Xiang, T.F. Jaramillo, A.Z. Weber, Gas-Diffusion Electrodes for Carbon Dioxide Reduction: A New Paradigm, ACS Energy Lett. 4 (2019) 317–324, https://doi.org/10.1021/acsenergylett.8b02035.
[18] E.W. Lees, B.A.W. Mowbray, F.G.L. Parlane, C.P. Berlinguette, Gas diffusion electrodes and membranes for CO2 reduction electrolysers, Nat. Rev. Mater. 7 (2022) 55–64, https://doi.org/10.1038/s41578-021-00356-2.
[19] K. Liu, W.A. Smith, T. Burdyny, Introductory Guide to Assembling and Operating Gas Diffusion Electrodes for Electrochemical CO 2 Reduction, ACS Energy Lett. 4 (2019) 639–643, https://doi.org/10.1021/acsenergylett.9b00137.
[20] J. Li, H. Zeng, X. Dong, Y. Ding, S. Hu, R. Zhang, Y. Dai, P. Cui, Z. Xiao, D. Zhao, L. Zhou, T. Zheng, J. Xiao, J. Zeng, C. Xia, Selective CO2 electrolysis to CO using isolated antimony alloyed copper, Nat. Commun. 14 (2023), https://doi.org/10.1038/s41467-023-35960-z.
[21] F.P. García de Arquer, C.T. Dinh, A. Ozden, J. Wicks, C. McCallum, A.R. Kirmani, D.H. Nam, C. Gabardo, A. Seifitokaldani, X. Wang, Y.C. Li, F. Li, J. Edwards, L.J. Richter, S.J. Thorpe, D. Sinton, E.H. Sargent, CO2 electrolysis to multicarbon products at activities greater than 1 A cm−2, Science (80-.). 367 (2020) 661–666. https://doi.org/10.1126/science.aay4217.
[22] S. Pérez-Rodríguez, F. Barreras, E. Pastor, M.J. Lázaro, Electrochemical reactors for CO2 reduction: From acid media to gas phase, Int. J. Hydrogen Energy. 41 (2016) 19756–19765, https://doi.org/10.1016/j.ijhydene.2016.06.130.
[23] N. Gutiérrez-Guerra, L. Moreno-López, J.C. Serrano-Ruiz, J.L. Valverde, A. de Lucas-Consuegra, Gas phase electrocatalytic conversion of CO2 to syn-fuels on Cu based catalysts-electrodes, Appl. Catal. B Environ. 188 (2016) 272–282, https://doi.org/10.1016/j.apcatb.2016.02.010.
[24] J.B.K. and J.N. C. Delacourt, P. L. Ridgway, Design of an electrochemical cell making syngas (CO+H-2) from CO2 and H2O reduction at room temperature, J. Electrochem. Soc. 155 (2008) B42–B49.

[25] L. Hoof, N. Thissen, K. Pellumbi, K. Junge Puring, D. Siegmund, A.K. Mechler, U. P. Apfel, Hidden parameters for electrochemical carbon dioxide reduction in zero-gap electrolyzers, Cell Reports Phys. Sci. 3 (2022), 100825, https://doi.org/10.1016/j.xcrp.2022.100825.

[26] S. Alinejad, J. Quinson, G.K.H. Wiberg, N. Schlegel, D. Zhang, Y. Li, S. Reichenberger, S. Barcikowski, M. Arenz, Electrochemical Reduction of CO2 on Au Electrocatalysts in a Zero-Gap, Half-Cell Gas Diffusion Electrode Setup:a Systematic Performance Evaluation and Comparison to an H-cell Setup, ChemElectroChem. e202200341 (2022), https://doi.org/10.1002/celc.202200341.

[27] M.D.J. Gaìlvez-Vaìzquez, P. Moreno-García, H. Xu, Y. Hou, H. Hu, I.Z. Montiel, A. V. Rudnev, S. Alinejad, V. Grozovski, B.J. Wiley, M. Arenz, P. Broekmann, Environment matters: CO2RR electrocatalyst performance testing in a gas-fed zero-gap electrolyzer, ACS Catal. (2020), https://doi.org/10.1021/acscatal.0c03609.

[28] Y. Kong, M. Liu, H. Hu, Y. Hou, S. Vesztergom, M. de J. Gálvez-Vázquez, I. Zelocualtecatl Montiel, V. Kolivoška, P. Broekmann, Cracks as Efficient Tools to Mitigate Flooding in Gas Diffusion Electrodes Used for the Electrochemical Reduction of Carbon Dioxide, Small Methods 2200369 (2022), https://doi.org/10.1002/smtd.202200369.

[29] M. De Jesús Gálvez-Vázquez, S. Alinejad, H. Hu, Y. Hou, P. Moreno-García, A. Zana, G.K.H. Wiberg, P. Broekmann, M. Arenz, Testing a Silver Nanowire Catalyst for the Selective CO2 Reduction in a Gas Diffusion Electrode Half-cell Setup Enabling High Mass Transport Conditions, Chimia (aarau) 73 (2019) 922–927, https://doi.org/10.2533/chimia.2019.922.

[30] S. Alinejad, M. Inaba, J. Schröder, J. Du, J. Quinson, A. Zana, M. Arenz, Testing fuel cell catalysts under more realistic reaction conditions: accelerated stress tests in a gas diffusion electrode setup, Jphys Energy. 2 (2020), 024003, https://doi.org/10.1088/2515-7655/ab67e2.

[31] S. Alinejad, J. Quinson, J. Schröder, J.J.K. Kirkensgaard, M. Arenz, Carbon-Supported Platinum Electrocatalysts Probed in a Gas Diffusion Setup with Alkaline Environment: How Particle Size and Mesoscopic Environment Influence the Degradation Mechanism, ACS Catal. 10 (2020) 13040–13049, https://doi.org/10.1021/acscatal.0c03184.

[32] M. Ma, E.L. Clark, K.T. Therkildsen, S. Dalsgaard, I. Chorkendorff, B. Seger, Insights into the carbon balance for CO2 electroreduction on Cu using gas diffusion electrode reactor designs, Energy Environ. Sci. 13 (2020) 977–985, https://doi.org/10.1039/d0ee00047g.

[33] J. Schröder, J. Quinson, J.K. Mathiesen, J.J.K. Kirkensgaard, S. Alinejad, V. A. Mints, K.M.Ø. Jensen, M. Arenz, A New Approach to Probe the Degradation of Fuel Cell Catalysts under Realistic Conditions: Combining Tests in a Gas Diffusion Electrode Setup with Small Angle X-ray Scattering, J. Electrochem. Soc. 167 (2020), 134515, https://doi.org/10.1149/1945-7111/abbdd2.

[34] E.W. Lees, B.A.W. Mowbray, D.A. Salvatore, G.L. Simpson, D.J. Dvorak, S. Ren, J. Chau, K.L. Milton, C.P. Berlinguette, Linking gas diffusion electrode composition to CO2reduction in a flow cell, J. Mater. Chem. a. 8 (2020) 19493–19501, https://doi.org/10.1039/d0ta03570j.

[35] M.S. Wilson, S. Gottesfeld, Thin-film catalyst layers for polymer electrolyte fuel cell electrodes, J. Appl. Electrochem. 22 (1992) 1–7, https://doi.org/10.1007/BF01093004.

[36] S.P. Schwaminger, B. Begovic, L. Schick, N.A. Jumani, M.W. Brammen, P. Fraga-García, S. Berensmeier, Potential-Controlled Tensiometry: A Tool for Understanding Wetting and Surface Properties of Conductive Powders by Electroimbibition, Anal. Chem. 90 (2018) 14131–14136, https://doi.org/10.1021/acs.analchem.8b03475.

[37] K. Junge Puring, D. Siegmund, J. Timm, F. Möllenbruck, S. Schemme, R. Marschall, U.P. Apfel, Electrochemical CO2 Reduction: Tailoring Catalyst Layers in Gas Diffusion Electrodes, Adv. Sustain. Syst. 5 (2021) 1–13, https://doi.org/10.1002/adsu.202000088.